Available online at www.sciencedirect.com

ScienceDirect

Proceedings of the Combustion Institute 35 (2015) 3337–3345

Proceedings of the Combustion Institute

www.elsevier.com/locate/proci

Modeling heat loss effects in the large eddy simulation of a model gas turbine combustor with premixed flamelet generated manifolds

F. Proch [a,*], A.M. Kempf [a,b]

[a] Institute for Combustion and Gasdynamics (IVG), Chair for Fluid Dynamics, University of Duisburg-Essen, 47048 Duisburg, Germany

[b] Center for Computational Sciences and Simulation (CCSS), University of Duisburg-Essen, 47048 Duisburg, Germany

Available online 12 August 2014

Abstract

Large eddy simulation results are presented for a model gas turbine combustion chamber, which is operated with a premixed and preheated methane/air mixture. The off-center position of the high axial momentum confined jet burner causes a strong outer recirculation, which stabilizes the flame. Turbulent combustion is modeled by the premixed flamelet generated manifolds (PFGM) technique, which is combined with the artificial thickened flame (ATF) approach. The influence of different heat loss modeling strategies on flame propagation and structure is investigated. Besides the established method of using burner-stabilized flames as basis for the non-adiabatic tabulation, an alternative approach based on freely propagating flames with heat loss inclusion by scaling of the energy equation source term is presented. Different grid resolutions are applied to study the impact of cell size and filter width on the results, the effect of subfilter modeling is also examined. The simulation setup and the modeling approach are validated by comparison of computed statistics against measurements. A good overall agreement between simulation and experiment is observed. However, the length of the flame was slightly under-predicted; it is shown that a simple method for consideration of strain effects on the flame has the potential to improve the predictions here. The effect of heat loss on the combustion process is then characterized further based on probability density functions obtained from the simulation results.

Keywords: Large eddy simulation; Confined jet flame; Turbulent premixed combustion; Tabulated chemistry; Heat losses

1. Introduction

Concepts for modern gas turbine combustors often feature regions with (partially) premixed combustion, which are exposed to significant heat loss. Large eddy simulation (LES) has proven in the past to be a very capable approach for the numerical simulation of such devices.

Different methods have been established for the modeling of premixed combustion within LES, for example based on tracking of the flame front by the G-equation model [1–3] or modeling of the flame surface density (FSD) [4,5]. Another

* Corresponding author. Address: Carl-Benz Straße 199, 47057 Duisburg, Germany. Fax: +49 203 379 8102.
E-mail address: fabian.proch@uni-due.de (F. Proch).

http://dx.doi.org/10.1016/j.proci.2014.07.036
1540-7489/

group of models is based on widening of the flame in normal direction by means of either filtering [6–8] or artificial thickening (ATF) [9,10]; the latter approach is applied here. The combustion progress and flame propagation are described through the premixed flamelet generated manifolds (PFGM) technique [11–13]. These approaches are all derived for adiabatic conditions in their basic formulation, and need to be extended by heat loss effects for the proper computation of confined geometries. Heat loss due to radiation has been considered for example by Marracino and Lentini [14], by Ihme and Pitsch [15], by Franchetti et al. [16] and by Schmitt et al. [17]. Fiorina et al. [18] suggested the computation of burner stabilized one-dimensional flames and to use the tabulated results for correcting the source term and the flame speed. This approach has been applied within the RANS [19] and the LES [20,21] context.

The present work aims to model and investigate the influence of the heat loss on the LES results in the lean premixed combustion regime. Three different models are compared to the adiabatic reference solution: First a very simple model where the heat loss only affects the temperature and the transport coefficients, secondly the model by Fiorina et al. [18], and thirdly an approach with non-constant heat loss inside the flame.

To properly judge the model behavior, a test case with a significant amount of heat loss was required, which was found in a confined laboratory scale burner investigated at DLR Stuttgart by Lammel and coworkers [22]. Its jet-nozzle exit is arranged in an off-center position, resulting in a strong recirculation of the hot combustion products, which stabilizes the flame and causes strong heat loss to the burner walls. We consider a configuration with values of 90 m/s, 0.71 and 573 K for the bulk inflow velocity, the equivalence ratio of the premixed methane/air mixture and the temperature at the inlet, respectively. This burner has also been investigated with RANS by Donini et al. [19], and with hybrid RANS/LES by Di Domenico et al. [23].

2. Modeling approach

In the PFGM approach [11,12], one dimensional freely propagating flames are computed with a detailed chemical mechanism. The results are mapped over a small subset of control variables and subsequently stored in a low dimensional lookup-table, which is accessed by the CFD solver. In the present work, the one dimensional flame computations are carried out with the software library Cantera [24] for the GRI-3.0 [25] mechanism. A unity Lewis number assumption for all species is used, which required the implementation of an additional transport model into Cantera. The reaction progress is described by the species mass fraction sum $Y_C = Y_{CO_2} + Y_{CO} + Y_{H_2O} + Y_{H_2}$. We found that this progress variable definition works well for methane/air over the whole flammability range, although both simpler and more complex formulations exist.

2.1. Inclusion of heat loss in PFGM

To include the heat loss into the PFGM, the sum of sensible and chemical enthalpy $h = h_s + \sum_{k=1}^{N} \Delta h_{f,k}^0 Y_k$ is used as second progress variable. As mentioned above, different methods are used to generate the non-adiabatic PFGM table:

For the first method (**M1**) only the adiabatic free flame without heat loss is computed. Afterwards the gas temperature is successively reduced from the adiabatic to the ambient temperature. The gas composition, the laminar flame speed, the laminar flame thickness and the reaction rate are kept constant. The heat loss influences the solution by reducing the temperature which alters the density and the transport coefficients.

The second method (**M2**) relies on the computation of burner stabilized flames [18]. At the inlet of the domain, constant values are prescribed for the mass flow and the temperature. By setting a lower mass flow, a higher level of heat loss over the entire flame is induced. Although the underlying assumption of temperature independence of the heat loss is unlikely to hold entirely in a real flame, this approach has been used with good success for the prediction of the flame behavior as well as the inner flame structure by Fiorina et al. [18], Cecere et al. [20], Ketelheun et al. [21] and Donini et al. [19]. Outside the flammability region, the temperature is reduced corresponding to M1, this time not starting from the adiabatic flame but from the burner-stabilized flamelet with the maximum heat loss. As it was found that the results of the CFD simulations performed within this work were insensitive to the exact value of the flammability limit, it was assumed that it is reached when the flame speed falls below 0.05 m/s.

The third method (**M3**) is based on introducing heat loss into a freely propagating flame. This is achieved by scaling the energy equation source term due to chemical reaction by a constant factor $(1 - f_L)$ over the whole flame. The modified energy equation that was implemented in Cantera reads:

$$\dot{m}\, c_p \frac{\partial T}{\partial z} = \frac{\partial}{\partial z}\left(\lambda \frac{\partial T}{\partial z}\right) - \sum_{k_1}^{K} c_{pk} j_{k,z} \frac{\partial T}{\partial z} - \boxed{(1 - f_L)} \sum_{k_1}^{K} h_k \dot{\omega}_k W_k \tag{1}$$

In Eq. (1), $\dot{m}, c_p, \lambda, \dot{\omega}_k, W_k$ and $j_{k,z}$ denote the mass flow, heat capacity, thermal conductivity, reaction rate, molecular weight and the diffusive mass flux of species k in z-direction, respectively. The second term on the RHS of Eq. (1) represents the energy changes due to differential diffusion, thus it cancels out for the applied unity Lewis number approach. Starting with the adiabatic flame ($f_L = 0$), different flames with successively raised values of f_L are computed to cover the whole range of enthalpy defects until the flame speed value of 0.05 m/s used as the flammability limit is reached at a value of $f_L = 0.5$. For higher enthalpy defects, the temperature is reduced as for the first two methods, starting from the flamelet at the flammability limit ($f_L = 0.5$). This model results in a nearly linear relationship between the heat loss and the temperature over the flame. This promises to be a more suitable approximation of the real physical behavior, since the strength of sources of heat loss as conduction along the flame front and radiation is depending on the temperature. Furthermore, the assumption of a heat sink at the unburned side of the flame is avoided, which is somewhat questionable in an aerodynamically stabilized flame. Consequently, the flame trajectories no longer describe vertical lines in the h-Y_C diagram, which results in a modified modeling strategy than for M1 and M2. The term $f_L \sum_{k_1}^{K} h_k \dot{\omega}_k W_k$ needs to be included as sink term in the energy equation, it is stored as an additional quantity inside the PFGM table. To improve the resolution and simplify the lookup within the CFD code, the two control variables h and Y_C are normalized:

$$h_N = \frac{h - h^{min}(Y_C)}{h^{max}(Y_C) - h^{min}(Y_C)} \tag{2}$$

$$C = \frac{Y_C - Y_C^{min}(h)}{Y_C^{max}(h) - Y_C^{min}(h)} \tag{3}$$

The resulting manifold is then mapped onto an equidistant h_N-C grid by bilinear interpolation, the minimum and maximum values of $h(Y_C)$ and $Y_C(h_N)$ are also mapped in the same way and stored for usage inside the CFD simulation.

A comparison of the laminar flame speed and flame thickness as a function of the heat loss for M2 and M3 is shown in Fig. 1, the adiabatic solution (**AD**) is shown as reference. Also included is a comparison of the resulting flame structure for the respective flame with maximum heat loss. The laminar flame speed s_l^0 is reduced more by the heat loss for M2 than for M3, therefore the necessary heat loss to reach the minimum flame speed is about 10% larger for M3. The laminar flame thickness δ_l^0 is growing stronger with heat loss for M3 than for M2, most obvious towards the extinction limit. As already mentioned, the heat loss is increasing almost linearly with the temperature for M3, whereas it stays constant for M2.

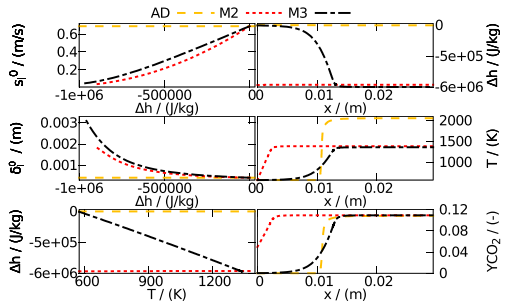

Fig. 1. Comparison of global flame properties and resulting flame structure for M2 and M3, the adiabatic solution AD is shown as reference.

The flame structure of the respective flame with maximum heat loss for M2 and M3 is compared to the adiabatic case AD in the plots on the right side of Fig. 1. The temperature dependent heat loss for M3 results in a smooth reduction of the enthalpy over the flame. The temperature profile for M3 has longer preheating and oxidation zones and a significantly lower peak temperature compared to AD, nevertheless the general flame position marked by the point of inflection is maintained. For M2, the flame structure differs significantly from AD and M3, the temperature increases to its final value that is comparable to M3 rapidly at the beginning of the domain and stays constant afterwards. The behavior in temperature is basically also mirrored by the mass fraction of CO_2, with the exception that the final value is not affected by the heat loss and is identical for all three cases. On the unburned side of the flame, at ambient temperature, M2 predicts a significant mass fraction of CO_2 in contrast to M3 and AD.

2.2. ATF model

The typical thickness of a premixed flame (0.1–0.5 mm) is not properly resolved on practically affordable LES grids with cell sizes bigger than 0.5 mm. To tackle this problem, the ATF approach artificially thickens the flame by introducing a thickening factor F into the transport equations for enthalpy and progress variable:

$$\frac{\partial \bar{\rho}\tilde{h}}{\partial t} + \frac{\partial}{\partial x_i}\left(\bar{\rho}\tilde{u}_i\tilde{h}\right) = \frac{\partial}{\partial x_i}\left(\left[FE\frac{\lambda}{c_p} + (1-\Omega)\frac{\mu_t}{\mathrm{Sc}_t}\right]\frac{\partial \tilde{h}}{\partial x_i}\right) + \frac{E}{F}\dot{\omega}_h \tag{4}$$

$$\frac{\partial \bar{\rho}\tilde{Y}_C}{\partial t} + \frac{\partial}{\partial x_i}\left(\bar{\rho}\tilde{u}_i\tilde{Y}_C\right) = \frac{\partial}{\partial x_i}\left(\left[FE\bar{\rho}D_C + (1-\Omega)\frac{\mu_t}{\mathrm{Sc}_t}\right]\frac{\partial \tilde{Y}_C}{\partial x_i}\right) + \frac{E}{F}\dot{\omega}_C \tag{5}$$

In Eqs. (4) and (5), $\rho, u_i, \lambda, c_p, D_c, \dot{\omega}_C, \mu_t$ and Sc_t represent the fluid density, flow velocity, thermal

conductivity, heat capacity, progress variable diffusion coefficient, progress variable reaction rate, turbulent viscosity and turbulent Schmidt number, respectively. The source term for the enthalpy $\dot{\omega}_h$ represents the heat loss for M3 as described above, and becomes zero for M1 respectively M2. To avoid unphysical effects of the thickening procedure in regions without combustion, F is only applied inside the flame region characterized by high gradients of the progress variable [26]. The flame region is detected with the flame sensor Ω, which is computed from the dimensionless progress variable gradient of the one-dimensional Cantera flame computations [27]:

$$\Omega(C,h) = \left[\frac{\frac{dY_C(x)}{dx}}{\max\left(\frac{dY_C(x)}{dx}\right)}\right]_{1-D} \tag{6}$$

The actual value of the thickening factor is then computed from:

$$F = 1 + \Omega(F_{max} - 1) \tag{7}$$

with

$$F_{max} = \max\left(\frac{n\Delta_{mesh}}{\delta_l^0}, 1\right) \tag{8}$$

In Eq. (8), Δ_{mesh} represents the mesh cell size and n the number of grid points on which the flame thickness is resolved, it is set to a value of 5 following a suggestion by Charlette et al. [10]. The flame thickness is computed based on the maximum gradient of the temperature profile from the one-dimensional computations, T_b and T_u denote the temperature on the burned and unburned side, respectively:

$$\delta_l^0 = \frac{T_b - T_u}{\max\left(\frac{dT}{dx}\right)} \tag{9}$$

The effect of the velocity fluctuations on the subfilter level is modeled with the efficiency function E, which is evaluated from the analytical formulation of Charlette et al. [10], which is used with the corrections suggested by Wang et al. [28]. The respective modeling constant was set to the commonly used value of $\beta = 0.5$ [10]. The detailed formulation of the model has been omitted for brevity, it can be found in the available literature [10,27,28].

The influence of radiation was neglected, as simulations with a simple radiation model showed that the related effects are one order of magnitude smaller than those of the convective heat transfer.

3. Experimental and numerical configuration

3.1. Experiment

The high-velocity preheated and premixed combustor has a rectangular cross section with a width of 5 and a depth of 4 nozzle diameters, the jet nozzle is mounted in an off-center position. The walls are made from Quartz to provide optical access. The geometrical setup and the boundary conditions are shown in Fig. 2. Velocity fields have been obtained from PIV measurements; profiles of species mole fractions and temperature were determined from Raman scattering measurements by Lammel et al. [22].

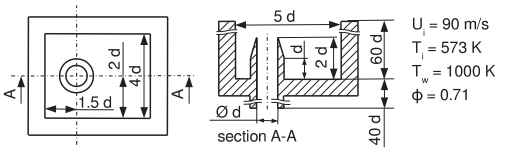

Fig. 2. Geometrical burner setup and boundary conditions, the computational domain is shown in Fig. 3.

The wall temperatures have not been measured during the experiment. However, according to O. Lammel the quartz glass surface would melt at approximately 1000 °C, crystallization of the glass starts at around 650 °C. Based on the aging behavior of the glass, the wall temperature was estimated in-between 650 °C and 800 °C (O. Lammel, personal communication, November 2013), so we have rounded the temperature to 1000 K.

3.2. Numerical setup and CFD-solver

Computations are carried out with the in-house LES-solver 'PsiPhi' [16,27,29,30]. Solved are the Favre-filtered governing equations for mass, momentum, progress variable and enthalpy in low-Mach number formulation. Time integration is performed with a low-storage third order Runge–Kutta scheme, the parallelization is carried out using a distributed-memory message passing interface (MPI) domain decomposition. The finite volume method (FVM) is used to discretize the equations on an equidistant Cartesian grid. Convective fluxes are interpolated with a central difference scheme for momentum, for scalar quantities and density a total variation diminishing (TVD) scheme with the non-linear CHARM limiter [31] is applied. The geometry is described by immersed boundaries.

The effect of subfilter transport on momentum and scalar fields is considered with the eddy-viscosity and eddy-diffusivity approach, respectively. The turbulent Schmidt number is adjusted to 0.7, the turbulent viscosity is computed with the σ-model by Nicoud et al. [32], the respective modeling constant is set to $C_m = C_\sigma = 1.5$. This model gives the correct decrease of the turbulent viscosity within the near wall region, avoiding the need for a special wall treatment as required with the classical Smagorinsky model. A turbulent velocity profile with a mean value according to Fig. 2 is set at the inflow. Pseudo-turbulent fluctuations with a

length scale of 0.1 d and an intensity of 9 m/s are superimposed, they are generated using a version of the filtering method of Klein et al. [33,34]. The influence of the magnitude and the length scale of the fluctuations on the results was studied and found to be very small. Zero gradient boundary conditions are adjusted at the outlet for all quantities, where clipping avoids entrainment during start-up. The temperatures of the walls are fixed at 1000 K. The sensitivity of the results against a variation of this temperature was found to be negligible; flame position and length were not affected. Based on the conditions at the inlet, the combustion process falls into the thin reaction zones regime of the modified Borghi diagram.

The computational domain has a length of 24 d, the cell size is 0.1 d (nozzle diameter resolved by 10 cells) on the coarse and 0.025 d (nozzle diameter resolved by 40 cells) on the fine grid. This results in a total domain size of 38 (0.6) million cells and a computational time of 95,000 (280) CPU hours on the fine (coarse) grid. The sampling for the flow statistics was started after 10 flow-through times based on the bulk velocity and performed for another 20 flow-through times to consider the slow but important recirculating zone on the "right" side of the jet. Tests on the coarse grid have shown that this amount of sampling time is required and sufficient for accurate statistics.

4. Results and discussion

A first impression of the resulting flow and heat loss fields is given by Fig. 3, which shows instantaneous and mean contour plots of the axial velocity and the enthalpy loss for M3 on the fine grid (M3F). The structure of the axial velocity field is dominated by a large recirculation zone developing on the "right" side of the domain. Smaller recirculation zones develop at the "lower left" part of the domain and "in front of" as well as "behind" the jet. The main jet starts breaking up after half a nozzle diameter, which induces turbulent fluctuations that are dissipated further downstream. The mean jet is bend to the "right" near the end of the domain and feeds the recirculation zone.

The enthalpy defect is strongest in the lower part of the domain, where recirculated burned gases have been cooled down by around 700 K in comparison to the adiabatic solution MA due to heat exchange with the chamber walls. The reduction of the flame speed by the effect of heat loss results in local extinction near the burner exit.

Radial profiles of velocity and temperature [22] are presented in Figs. 4 and 5, comparing the results for the adiabatic reference solution and the models described above on the coarse (C) and fine (F) grid.

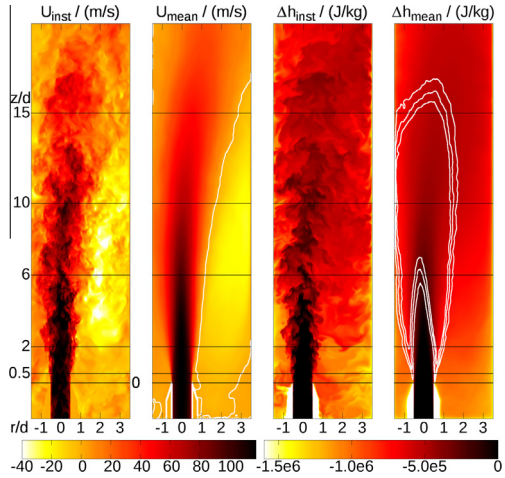

Fig. 3. Instantaneous and mean contour plots of axial velocity (left) and enthalpy loss (right) in a burner cross section obtained on the fine grid (M3F). In the mean plots, white isolines denote zero velocity (left) respectively the flame sensor which marks the combustion region (right).

The axial velocity statistics in Fig. 4 are in good agreement with the measurements for M2 and M3, whereas AD and M1 struggle to predict the velocity and the correct position of the recirculation zone. This trend is mirrored in the fluctuation profiles, which are initially under-predicted by AD and M1 and then dissipate too late. Near the nozzle exit, no significant differences between the velocity predictions of the individual models can be observed. The velocity predictions do not improve significantly with grid refinement, implying sufficient grid resolution.

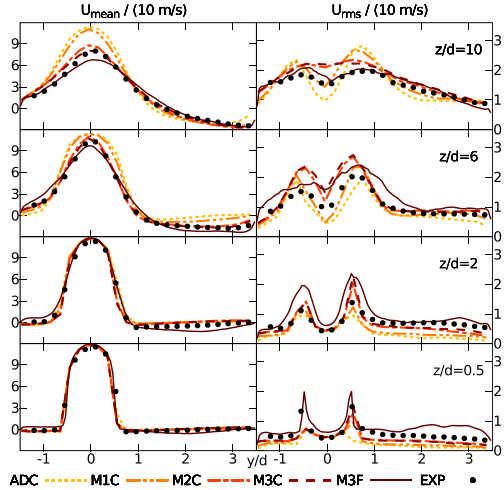

Fig. 4. Radial profiles of the mean and rms of axial velocity at different downstream locations.

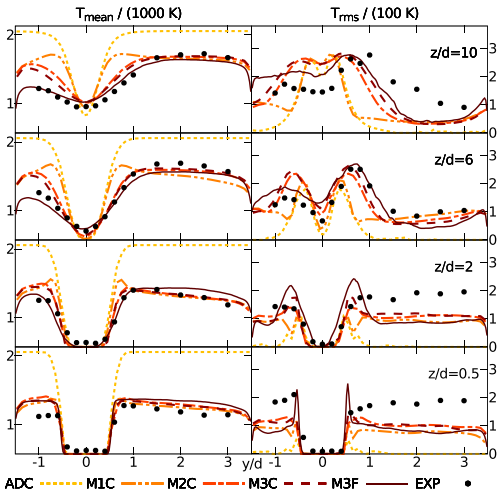

Fig. 5. Radial profiles of the mean and rms of temperature at different downstream locations.

As a result of the significant amount of heat loss visible in Fig. 3, the peak temperatures for the adiabatic simulation AD in Fig. 5 exceed the measured ones by several hundred Kelvin. In contrast to that, M1 matches the peak temperatures of the experiment, but under-predicts the thickness of the flame. M2 and M3 basically match the mean temperature measurements, some deviations occur towards the "left" burner wall. The predictions here improve with M3 compared to M2 and with grid refinement. The latter can be explained by the fact that the higher temperature gradients in this region can be resolved more adequately on the fine grid. Except for AD, all other methods are able to reproduce the temperature fluctuations within the burned gas qualitatively. However, the strength of the fluctuations is under-predicted near the burner exit. Physically it seems unlikely that the temperature fluctuations within the recirculation zone, which mainly consists of burned products, should be as high as in the flame region.

4.1. Strain correction

Although the measured temperature field is captured well by the simulation, it turned out that all methods under-predicted the length of the flame to a certain degree. To evaluate if this is related to the relatively high axial velocity magnitude, the tabulation method M3 is extended by a simple strain correction (**M3S**) based on Cantera premixed counterflow flames [35]. One stream represents the hot exhaust gas and the other one the cold unburned mixture from the respective free flame computations. These computations have been carried out for different amounts of heat loss and varying compressive strain rates, where the energy equation was computed according to Eq. (1) and the flame speed was evaluated from:

$$s_L^0 = \frac{1}{\rho_u Y_{\mathrm{CO_2},b}} \int_{-\infty}^{\infty} \dot{\omega}_{\mathrm{CO_2}} dx \tag{10}$$

In Eq. (10), ρ_u, $Y_{\mathrm{CO_2},b}$ and $\dot{\omega}_{\mathrm{CO_2}}$ denote the density of the unburned mixture, mass fraction of CO_2 in the exhaust gas and reaction rate of CO_2, respectively. Figure 6 shows the resulting flame speed as a function of the maximum strain rate, the plot has been normalized by the flame speed of the respective free flame. The Favre-filtered strain in the CFD computation is computed according to [1], with the flame normal vector $\tilde{n}_i$ pointing into the fresh mixture:

$$S = -\tilde{n}_i \frac{\partial \tilde{u}_i}{\partial x_j} \tilde{n}_j \quad \text{with} \quad \tilde{n}_i = -\frac{\frac{\partial \widetilde{Y_C}}{\partial x_i}}{\left|\frac{\partial \widetilde{Y_C}}{\partial x_i}\right|} \tag{11}$$

The obtained strain value is then normalized by the flame speed of the respective free flame, subsequently the correction factor is evaluated from the exponential fit given in Fig. 6 and applied to the progress variable reaction ratio, the flame speed and the flame sensor. As the basis of the fit are the maximum strain rates from the counterflow computations and only the resolved strain rate is taken into account, the described procedure represents a lower limit of the influence of the strain on the flame propagation.

Figure 7 shows the comparison of mean value and fluctuations of temperature and carbon dioxide at the most downstream measurement location. The strain correction improves the predictions notably, most visible towards the "left" side of the domain, the resulting flame length is in agreement with the measurements. However, the impact on the temperature profile seems to be a little bit too high towards the wall, which likely indicates that the correction should not be applied near the wall inside the boundary layer, where high strain rates may occur even in the absence of burned (and cooled down) products. Although the use of the correction improved the results significantly, it must be stressed that the development of this method should not be seen as finalized, and that further investigation on the

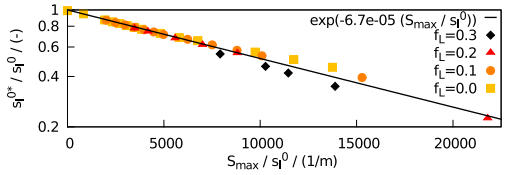

Fig. 6. Strain correction factor for different amounts of heat loss from Cantera premixed counterflow flames (symbols) and the respective exponential fit (line).

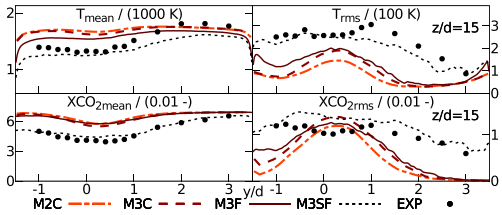

Fig. 7. Radial profiles of the mean and rms of temperature and carbon dioxide molar fraction at the last measurement position.

effects of strain in such flames is required – ideally by DNS. It also remains to be investigated if the strain itself is the main physical reason for the reduction of the flame speed, or rather some closely related phenomenon like internal exhaust gas recirculation, as suggested by Di Domenico et al. [23]. Di Domenico et al. [23] also found no evidence for a relevant contribution of auto ignition on the flame stabilization – even for a faster jet (bulk velocity of 150 m/s).

4.2. Analysis of the heat loss

Figure 8 compares the normalized PDF of the reaction source term conditional Favre-filtered enthalpy defect for the different models and grid resolutions, AD and M1C are skipped for brevity. In all cases combustion is found over a wide enthalpy range which starts at an enthalpy defect of approximately −0.2 MJ/kg on the fine and −0.4 MJ/kg on the coarse grids, respectively. The distributions show a negative skewness with a long tail towards low enthalpies. This can be attributed to the fact that the flame gets more sensitive to small disturbances when approaching the extinction limit, resulting in a stronger influence of the turbulent velocity fluctuations on the flame behavior. To study the influence of the subfilter contribution, two additional simulations have been carried out for M3C with an additional top-hat FDF closure in enthalpy respectively progress variable [27,36,37]. The resulting impact on the source term PDFs (and also on the flow statistics) is very small, the amount of resolved source term is approximately identical. M2C predicts a smaller amount of heat release at the decreasing side of the distribution compared to M3C, which results in a lower amount of resolved source term. In the fine grid simulation M3F around 95% of the flame is resolved, the peak value of heat release is shifted towards lower enthalpies compared to the coarse grid simulations. The fine grid predicts a larger amount of combustion towards the extinction limit than the coarse one. An explanation for this behavior is that most of the flames near the extinction limit are found in the near-wall region at the "left" side of the burner, which is resolved better on the fine grid. The efficiency function E reduces to unity at low enthalpy values due to the increase of flame thickness shown in Fig. 1, indicated by matching of the resolved and total source term. The strain correction (M3SF) reduces the skewness and width of the distribution noticeably, which can be explained by flame blow off near the flammability limit by the effect of mean flow strain rate. Thus the probability for re-ignition of these flames is reduced drastically, causing a shift of the combustion process to more stable regions with higher enthalpy values.

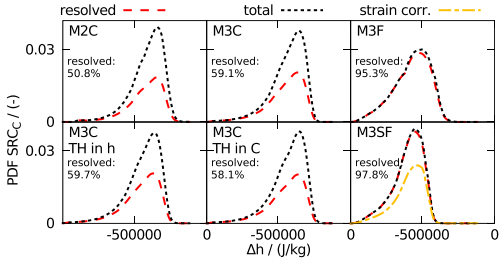

Fig. 8. Normalized PDF of the Favre-filtered reaction source term conditional on Favre-filtered enthalpy defect over the entire domain for the presented models. Results are also shown for M3C with an additional top-hat (TH) subfilter model in enthalpy and progress variable, respectively. Shown are the total and the resolved reaction source term, the latter is obtained with an efficiency function of unity ($E = 1$ in Eq. (5)). The ratio of the integrated resolved source term and the integrated total source term is also given. For M3SF the total source term after the strain correction is also included.

5. Conclusions

A high velocity confined jet burner has been investigated with different methods for the inclusion of heat loss in PFGM. Considering the heat loss was necessary as the adiabatic reference simulation (AD) over-predicted the temperature by several hundred Kelvin and failed to predict the flow field correctly. The combination of an adiabatic combustion model with the solution of the energy equation (M1) was able to predict the correct peak values of the temperature, but neither the correct flame shape and length nor the correct velocity field.

To capture the shape of the flame and the correct velocity field, it was necessary to consider the effect of the heat loss on the flame structure and propagation velocity. Two methods based on Cantera computations with detailed chemistry have been compared, an established one based on burner stabilized flames (M2) and one based on scaling of the energy equation source term (M3). Both methods performed well and lead to

very comparable results. The new method yielded slight improvements in the predictions of temperature towards the "left" burner wall and of velocity further downstream. Only a small improvement of the results with grid refinement was found (M3F), mostly visible for the temperature due to better resolution of the wall boundary layer. The predictions on the coarse grid showed a very satisfactory agreement with the measurements for M2 and M3.

Even though the last two models were able to predict the flame structure and the flow field, they still under-predicted the flame length by some degree. It was shown that inclusion of a simple strain correction method (M3SF) improves the prediction of the flame length. However, the exact formulation of this model and the details of the underlying physical mechanism require further investigation.

By analyzing and comparing the PDF of the source term conditional on the heat loss for the different models, it was shown that the combustion process takes place over a wide range of enthalpy defect. The probability of combustion towards the extinction limit is increased on the fine grid, implying that the respective parts of the flame are mainly located near to the "left" wall of the burner, where the effect of the grid refinement is strongest.

Acknowledgments

The authors gratefully acknowledge funding from the state of Nordrhein-Westfalen, Germany. Computations have been carried out using the DFG supported HPC resources of the Center for Computational Sciences and Simulation (CCSS) of the University of Duisburg-Essen, Germany. We would like to thank DLR Stuttgart and Siemens Energy for providing the experimental data. We further thank Dr. Wolfgang Meier, Dr. Oliver Lammel and Stefan Dederichs for many helpful discussions.

References

[1] N. Peters, *Turbulent Combustion*, Cambridge University Press, 2000.
[2] H. Pitsch, *Combust. Flame* 143 (2005) 587–598.
[3] M. Düsing, A.M. Kempf, F. Flemming, A. Sadiki, J. Janicka, *Prog. Comput. Fluid Dyn.* 5 (2005) 363–374.
[4] C. Angelberger, D. Veynante, F. Egolfopoulos, T. Poinsot, *Proceedings of the Summer Programm*, Center for Turbulence Research, Stanford, 1998, pp. 61–82.
[5] T. Ma, O. Stein, N. Chakraborty, A.M. Kempf, *Combust. Theory Model.* 17 (2013) 431–482.
[6] M. Boger, D. Veynante, H. Boughanem, A. Trouve, *Proc. Combust. Inst.* 27 (1998) 917–925.
[7] J. Galpin, A. Naudin, L. Vervisch, C. Angelberger, O. Colin, P. Domingo, *Combust. Flame* 155 (2008) 247–266.
[8] B. Fiorina, R. Vicquelin, P. Auzillon, N. Darabiha, O. Gicquel, D. Veynante, *Combust. Flame* 157 (2010) 465–475.
[9] O. Colin, F. Ducros, D. Veynante, T. Poinsot, *Phys. Fluids* 12 (2000) 1843–1863.
[10] F. Charlette, C. Meneveau, D. Veynante, *Combust. Flame* 131 (2002) 159–180.
[11] J.A. van Oijen, L.P.H. de Goey, *Combust. Sci. Technol.* 161 (2000) 113–137.
[12] J.A. van Oijen, R.J.M. Bastiaans, L.P.H. de Goey, *Proc. Combust. Inst.* 31 (2007) 1377–1384.
[13] G. Kuenne, A. Ketelheun, J. Janicka, *Combust. Flame* 158 (2011) 1750–1767.
[14] B. Marracino, D. Lentini, *Combust. Sci. Technol.* 128 (1997) 23–48.
[15] M. Ihme, H. Pitsch, *Phys. Fluids* 20 (2008) 055110.
[16] B.M. Franchetti, F.C. Marincola, S. Navarro-Martinez, A.M. Kempf, *Proc. Combust. Inst.* 34 (2013) 2419–2426.
[17] P. Schmitt, T. Poinsot, B. Schuermans, K. Geigle, *J. Fluid Mech.* 570 (2007) 17–46.
[18] B. Fiorina, R. Baron, O. Gicquel, D. Thevenin, S. Carpentier, N. Darabiha, *Combust. Theory Model.* 7 (2003) 449–470.
[19] A. Donini, S.M. Martin, R.J.M. Bastiaans, J.A. van Oijen, L.P.H. de Goey, Proceedings of the ASME Turbo Expo 2013.
[20] D. Cecere, E. Giacomazzi, F. Picchia, N. Arcidiacono, F. Donato, R. Verzicco, *Flow Turbul. Combust.* 86 (2011) 667–688.
[21] A. Ketelheun, G. Kuenne, J. Janicka, *Flow Turbul. Combust.* 91 (2013) 867–893.
[22] O. Lammel, M. Stöhr, P. Kutne, C. Dem, W. Meier, M. Aigner, *J. Eng. Gas Turbul. Power* 134 (2012), 041506-041506.
[23] M. Di Domenico, P. Gerlinger, B. Noll, Proceedings of the ASME Turbo Expo 2011.
[24] D.G. Goodwin, Cantera: an object-oriented software toolkit for chemical kinetics, thermodynamics, and transport processes, <http://code.google.com/p/cantera>, 2009.
[25] G.P. Smith, D.M. Golden, M. Frenklach et al., http://www.me.berkeley.edu/gri_mech, 2000.
[26] J.P. Legier, T. Poinsot, D. Veynante, *Proceedings of the Summer Programm*, Center for Turbulence Research, Stanford, 2000, pp. 157–168.
[27] F. Proch, A.M. Kempf, Combust. Flame (2014) <http://dx.doi.org/10.1016/j.combustflame.2014.04.010>.
[28] G. Wang, M. Boileau, D. Veynante, *Combust. Flame* 158 (2011) 2199–2213.
[29] F.C. Marincola, T. Ma, A.M. Kempf, *Proc. Combust. Inst.* 34 (2013) 1307–1315.
[30] M. Pettit, B. Coriton, A. Gomez, A.M. Kempf, *Proc. Combust. Inst.* 33 (2011) 1391–1399.
[31] G. Zhou, *Numerical Simulations of Physical Discontinuities in Single and Multi-fluid Flows for Arbitrary Mach Numbers, Ph.D. Thesis*, Chalmers University of Technology, Goteborg, Sweden, 1995.
[32] F. Nicoud, H.B. Toda, O. Cabrit, S. Bose, J. Lee, *Phys. Fluids* 23 (2011) 085106.

[33] M. Klein, A. Sadiki, J. Janicka, *J. Comput. Phys.* 186 (2003) 652–665.
[34] A.M. Kempf, S. Wysocki, M. Pettit, *Comput. Fluids* 60 (2012) 58–60.
[35] L. Tay Wo Chong, T. Komarek, M. Zellhuber, J. Lenz, C. Hirsch, W. Polifke, Proceedings of the European Combustion Meeting 4 (2009).
[36] J. Floyd, A.M. Kempf, A. Kronenburg, R.H. Ram, *Combust. Theory Model.* 13 (2009) 559–588.
[37] C. Olbricht, O.T. Stein, J. Janicka, J.A. van Oijen, S. Wysocki, A.M. Kempf, *Fuel* 96 (2012) 100–107.